Research Square

Preprints are preliminary reports that have not undergone peer review.
They should not be considered conclusive, used to inform clinical practice,
or referenced by the media as validated information.

Interfacial Tunneling Enables High-Gain SWIR Photodetection in Asymmetric n-i-n PbS Quantum Dot Devices

Bin Sun

iambsun@njupt.edu.cn

Nanjing University of Posts and Telecommunications https://orcid.org/0000-0002-8233-0999

Zeyao Han

Nanjing University of Posts and Telecommunications https://orcid.org/0009-0003-3748-3819

Boxiong Zhang

Nanjing University of Posts and Telecommunications

Chengjie Deng

Huazhong University of Science & Technology

Hua Zhang

Nanjing University of Posts and Telecommunications

Tao Meng

Nanjing University of Posts and Telecommunications

Mei Liu

Nanjing University of Posts and Telecommunications

Xingyi Li

Nanjing University of Posts and Telecommunications

Li Zhang

Nanjing University of Posts and Telecommunications

YUxuan Liu

Wuhan InRight Technology Co., Ltd.

Junyu Li

Southeast University

Mingyang Wei

National University of Singapore https://orcid.org/0000-0003-4820-2210

Liang Gao

Huazhong University of Science and Technology - Main Campus: Huazhong University of Science and Technology https://orcid.org/0000-0003-4391-8447

Article

Keywords:

Posted Date: November 4th, 2026

DOI: https://doi.org/10.21203/rs.3.rs-11369623/v1

License: This work is licensed under a Creative Commons Attribution 4.0 International License.
Read Full License

Additional Declarations: There is **NO** Competing Interest.

Interfacial Tunneling Enables High-Gain SWIR Photodetection in Asymmetric n-i-n PbS Quantum Dot Devices

Zeyao Han[1], *Boxiong Zhang*[1], *Chengjie Deng*[2], *Hua Zhang*[1], *Tao Meng*[1], *Mei Liu*[1], *Xingyi Li*[1], *Li Zhang*[1], *Yuxuan Liu*[3], *Junyu Li*[4], *Mingyang Wei*[5,*], *Liang Gao*[2,*], *Bin Sun*[1,*]

1 State Key Laboratory of Flexible Electronics (LoFE), Institute of Advanced Materials (IAM), School of Materials Science and Engineering, Nanjing University of Posts and Telecommunications (NJUPT), Nanjing 210023, PR China

2 Wuhan National Laboratory for Optoelectronics (WNLO) and School of Optical and Electronic Information, Huazhong University of Science and Technology, Wuhan 430070, P. R. China.

3 Wuhan InRight Technology Co., Ltd., Wuhan 430075, P. R. China.

4 Joint International Research Laboratory of Information Display and Visualization, School of Electronic Science and Engineering, Southeast University, Nanjing, 210096 China.

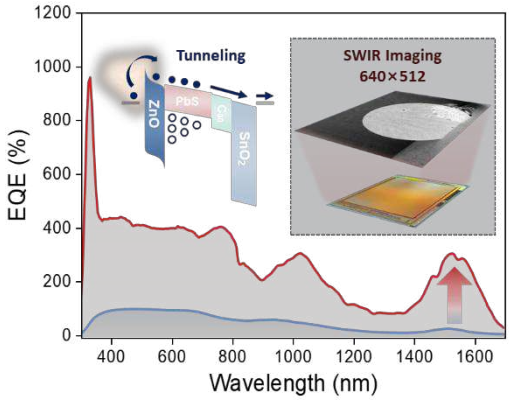
5 Department of Materials Science and Engineering, National University of Singapore, Singapore 117575, Singapore

*E-mail: highlight@hust.edu.cn, weimingy@nus.edu.sg, iambsun@njupt.edu.cn;

Abstract

Short-wave infrared (SWIR) sensing at 1500 nm is essential for eye-safe LiDAR and night vision. Conventional detectors fail in photon-starved environments due to systemic readout noise. Realizing photomultiplicative gain without amplifying noise or sacrificing response speed remains a bottleneck for colloidal quantum dot (CQD) detectors. Here, we report an asymmetric n-i-n CQD architecture that breaks this trade-off via interfacial band engineering. Integrating a C_{60} molecular interlayer establishes an energetically asymmetric junction that suppresses dark leakage while localizing accumulation of photogenerated holes. This accumulation acts as a dynamic gate, enhancing the local electric field and narrowing the electron-injection barrier to enable tunneling-mediated photomultiplication. The devices achieved a maximum external quantum efficiency (EQE) of over 1400% under -3.2 V and 300% at 1520 nm under -1.6 V, with a response time of 33 μs, and a dark-current density of 8×10^{-4} mA cm^{-2} at -0.5 V. Crucially, we monolithically integrated this architecture with a CMOS readout integrated circuit to demonstrate a 640×512-pixel focal-plane imaging under low-light conditions. These findings establish interfacial tunneling engineering as a promising strategy for combining high photomultiplicative gain, fast response, and CMOS-compatible integration in next-generation SWIR imaging systems.

Graphic abstract



Photons in the short-wave infrared (SWIR) region carry abundant spectral signatures, making SWIR detection indispensable for emerging technologies, including eye-safe LiDAR, machine vision, and non-invasive biomedical imaging[1-7]. Compared with photons shorter than 1300 nm, SWIR detection at 1500 nm permits higher peak power, which offers enhanced safety to human eyes and reduced scattering in biological tissues[8-10]. However, currently, the mainstream commercial sensing of 1500 nm light is still dominated by monolithic semiconductor devices (e.g., epitaxial InGaAs). As highlighted in recent works[11,12], these epitaxial technologies are fundamentally constrained by high manufacturing costs and the profound mismatch in heterogeneous integration with silicon readout integrated circuits (ROICs), severely impeding their further deployment in high-resolution, consumer-market imaging arrays.

To overcome these limitations, PbS colloidal quantum dots (CQDs) have emerged as a highly compelling alternative because of their solution processability, size-dependent bandgap, and straightforward CMOS compatibility[13-17]. In the past decades, extensive efforts in surface ligand engineering and device architecture optimization have pushed the specific detectivity of CQD photodiodes to impressive limits[13,18-23]. Nevertheless, while state-of-the-art p-n and p-i-n junction detectors exhibit excellent noise suppression, their sensitivity is fundamentally bounded by a unity-gain limit where the external quantum efficiency never exceeds 100%[24-26]. In photon-starved environments typical of long-range 1500 nm applications, the extremely weak output photocurrents generated by these unity-gain devices would fall below the background thermal fluctuations and the intrinsic noise of downstream readout circuits. Therefore, an internal gain mechanism that amplifies the optical signal above the readout noise floor before electronic readout is urgently needed.

To break this unity-gain limit, various photomultiplication strategies have been explored, mainly including avalanche multiplication, quantum tunneling, and trap-assisted charge injection[27,28]. Among them, the most widely adopted approach in CQD platforms relies on trap-assisted mechanisms[29-31]. For instance, early works by Konstantatos and colleagues demonstrated sensitive PbS CQD photodetectors by using deep-level interfacial states to capture minority carriers, thereby lowering the electron injection barrier and giving massive internal gain[32]. Although introducing deep-level interfacial states to capture minority carriers can yield substantial photomultiplication, this thermally activated process involves an inherent trade-off[33,34]. Specifically, long-lived traps prolong the response and degrade performance at low temperature because

of carrier freeze-out, limiting their practical deployment.

Alternatively, direct quantum tunneling and interfacial field-induced injection offer potential pathways for athermal and ultrafast multiplication[26,35,36]. For instance, interfacial hole-accumulation has been successfully utilized to trigger secondary electron injection in wide-bandgap organic photodiodes operating in the visible spectrum[37]. However, translating this field-driven concept into narrow-bandgap SWIR CQD architectures has proved difficult. To achieve sufficient barrier narrowing for electron tunneling, these conventional configurations typically require elevated external bias voltages. In narrow-bandgap semiconductors, such biases also promote unwanted dark carrier injection, increasing noise and undermining the detectivity gains afforded by photomultiplication, particularly under weak illumination and at microsecond response timescales[38,39].

Here we introduce an asymmetric n-i-n architecture that exploits the efficient n-type transport characteristics of halide-passivated CQD solids and the exceptional interfacial stability of wide-bandgap metal oxides. Specifically, by constructing a multilayered ITO/ZnO/PbS/C_{60}/SnO_2/Ag device, we establish an energetically asymmetric junction that breaks the interfacial symmetry. Rather than relying on conventional trap-assisted photomultiplication, the C_{60} molecular interlayer serves a dual function, facilitating electron extraction at the cathode while suppressing parasitic hole leakage. Under illumination, photogenerated holes accumulate at the ZnO/PbS injection interface, acting as a dynamic electrostatic gate that locally enhances the electric field and narrows the electron-injection barrier. This establishes a light-activated tunneling pathway that remains suppressed in the dark but enables efficient electron injection under illumination, even at relatively low operating biases. By decoupling localized field enhancement from the applied macroscopic electric field, this architecture enables athermal, tunneling-mediated photomultiplication while minimizing the accompanying increase in dark current. The asymmetric n-i-n architecture offers a promising route to overcoming the conventional gain-noise trade-off in SWIR photodetectors, and is compatible with monolithic integration into large-format SWIR focal-plane arrays.

Results and Discussion

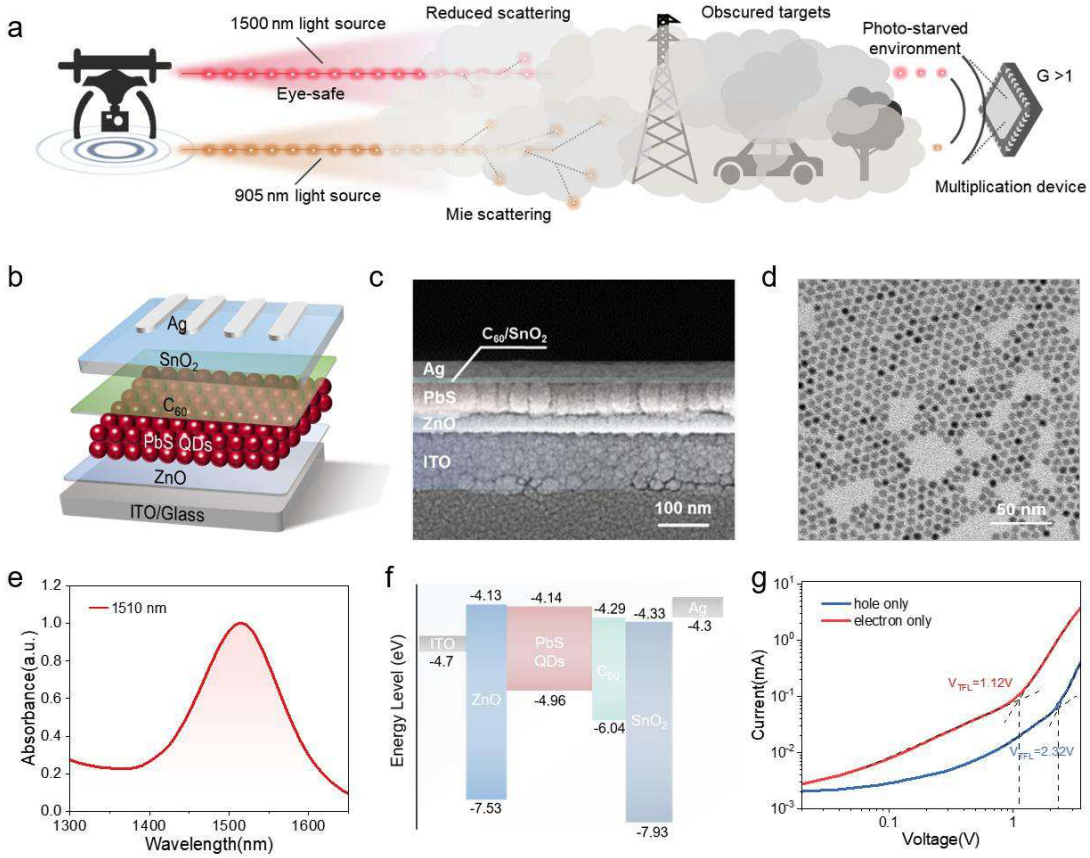


Figure 1. Device morphology, and material characterizations. (a) Schematic illustration of the advantages and applications of short-wave infrared (SWIR) multiplication detection. (b) Schematic illustration of the vertically stacked asymmetric n-i-n device architecture. (c) Cross-sectional scanning electron microscopy image showing the dense and planar layers. (d) Transmission electron microscopy image of the synthesized PbS colloidal quantum dots (CQDs). (e) Absorption spectrum of the PbS CQDs with the first exciton peak positioned at 1510 nm. (f) Energy band alignment diagram extracted from ultraviolet photoelectron spectroscopy measurements. (g) Space-charge-limited current measurements of the electron-only and hole-only PbS CQD devices.

SWIR sensing at 1500 nm is vital for eye-safe LiDAR and for operating in harsh environments. However, as illustrated in **Figure 1a**, the severely attenuated signals in such photon-starved conditions motivate the development of photodetectors with internal gain. Realizing photomultiplication in CQD detectors requires both a suitable energy band cascade that promotes photocarrier-induced injection while suppressing non-radiative recombination at bulk and interfacial defects. The asymmetric n-i-n detector proposed in this study adopts a vertically stacked multilayer architecture, as shown in **Figure 1b**. Compared with its p-i-p counterpart, the n-i-n configuration leverages the favorable electron transport properties of halide-passivated PbS CQD solids to establish an electron-dominated multiplication pathway. The wide-bandgap ZnO injection layer provides a substantial energetic barrier that suppresses thermionic

electron injection in the dark. Under illumination, however, photogenerated holes accumulate at the ZnO/PbS interface to facilitate quantum tunneling. The cross-sectional scanning electron microscopy (SEM) image in **Figure 1c** clearly reveals dense and planar contacts among the ITO/ZnO/PbS/C_{60}/SnO_2/Ag layers. Such high-quality, layer-by-layer deposition is a prerequisite for preventing local electrical breakdown and ensuring the uniformity of the tunneling interface. As the core of infrared photon harvesting, the PbS CQDs synthesized by hot injection are monodisperse. The transmission electron microscopy (TEM) image in **Figure 1d** gives an average diameter of about 6 nm. Benefiting from this precise size control and high crystallographic purity, their first exciton absorption peak is centered at 1510 nm, as shown in **Figure 1e**, perfectly covering the short-wave infrared window critical for optical fiber communications and eye-safe machine vision.

To further confirm the crystal structure and phase purity of the PbS quantum dots, X-ray diffraction (XRD) characterization was performed, as shown in **Supplementary Fig. 1**. The dominant diffraction peaks at 26.0°, 30.1°, 43.1°, and 51.0° are assigned to the (111), (200), (220), and (311) crystallographic planes of the PbS lattice, respectively. Furthermore, the absence of impurity peaks associated with lead oxide or other residual precursor across the entire measurement range confirms the high crystalline quality and phase purity of the PbS quantum dots. Subsequently, X-ray photoelectron spectroscopy (XPS) was utilized to investigate the chemical composition following ligand exchange (**Supplementary Fig. 2**). The distinct I 3d and Br 3d peaks confirm the complete replacement of initial long-chain organic ligands with inorganic halide anions. Meanwhile, the specific binding energies in the Pb 4f spectra verify the formation of robust chemical bonds between the electronegative halogens and uncoordinated surface lead atoms. This halide passivation effectively reduces dangling bonds and shortens the inter-nanocrystal coupling distance, lowering the density of deep-level traps that cause non-radiative recombination.

To evaluate the charge transport barriers within the films, ultraviolet photoelectron spectroscopy (UPS) was utilized to accurately determine the secondary electron cutoff edge and valence band onset of each functional layer, which can be found in **Supplementary Fig. 3**. Based on the extracted Fermi levels and work functions, the energy alignment diagram is constructed, as depicted in **Figure 1f**. A large energy step exists between the narrow-bandgap PbS and the wide-bandgap SnO_2. The insertion of the C_{60} layer leverages its deep valence band position (-6.04 eV) to establish a rigid

1.06 eV hole-blocking barrier at the cathode side. This barrier suppresses thermionic emission of photogenerated holes toward the silver electrode and confines them near the interface.

To estimate the trap density of the films, we measured the space-charge-limited current (SCLC) in the dark, as shown in **Figure 1g**. Specifically, electron-only (ITO/ZnO/PbS/ZnO/Ag) and hole-only (ITO/NiOx/PbS/MoO_3/Ag) devices were fabricated for this evaluation. Based on the extracted trap-filled limit voltage (V_{TFL}) and the theoretical relation:

$$n = \frac{2\varepsilon\varepsilon_0 V_{TFL}}{eL^2} \quad (1)$$

where n is the charge-trap density, ε, ε_0 represent the relative dielectric constant and the vacuum permittivity. e is the unit charge and L is the thickness of the film. The electron and hole trap densities of the PbS quantum dot film are calculated to be as low as 2.26×10^{16} cm^{-3} and 4.69×10^{16} cm^{-3}, respectively, which is consistent with effective surface passivation. This low density of Shockley-Read-Hall (SRH) recombination centers helps the device keep a low dark current even while operating at high gain.

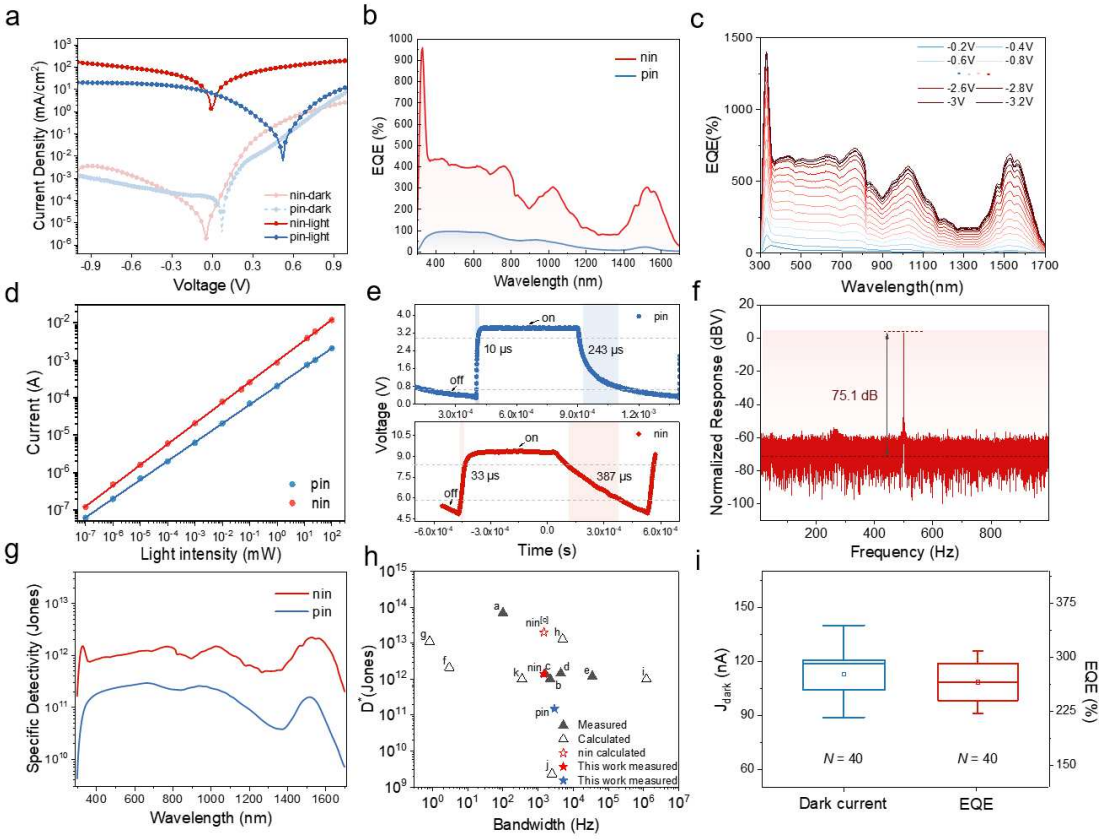


Figure 2. Optoelectronic performance of the asymmetric n-i-n photomultiplication detectors. (a) Dark and illuminated (AM1.5G) J-V curves of the n-i-n and conventional p-i-n devices. (b) External quantum efficiency (EQE) spectra of the n-i-n and p-i-n devices at -1.6 V bias. (c) Bias-

dependent EQE evolution of the n-i-n device from 0 V to -3.2 V. (d) Linear dynamic range of the n-i-n and p-i-n devices. (e) Transient response characteristics demonstrating the rise and fall times. (f) Signal-to-noise ratio of the n-i-n device under 500 Hz modulation. (g) Specific detectivity (D^*) of the n-i-n and p-i-n devices. (h) Benchmark of D^* against bandwidth for this work and representative SWIR CQD photodetectors. (i) Statistical distributions of dark current and EQE measured from 40 devices.

The combination of asymmetric band engineering and a low trap density gives this design an advantage over conventional p-i-n architectures. For a rigorous comparison, the control p-i-n device was constructed by replacing the bottom ZnO electron transport layer with a p-type NiOx hole transport layer. The J-V measurements in dark condition and under AM1.5G illumination in **Figure 2a** reveal that the asymmetric n-i-n device outputs a high photocurrent of 80 mA cm^{-2} at -0.5 V, with a dark current of 8×10^{-4} mA cm^{-2}, giving an extremely high on/off ratio of 10^5. In contrast, the conventional p-i-n device, which relies on charge separation within the depletion region, generates a photocurrent of only 18mA cm^{-2} under the same condition.

A direct comparison of the external quantum efficiency (EQE) spectra further quantifies this disparity, as shown in **Figure 2b**. At -1.6 V, the n-i-n device reaches an EQE of 300% at 1520 nm and surges to 957% in short-wavelength region. As a comparison, the maximum EQE of the p-i-n device is strictly limited to 94%, and to only 21% at 1520 nm. The corresponding responsivity curves are presented in **Supplementary Fig. 4**. The corresponding responsivity of the p-i-n device is therefore limited to 0.25 A/W at 1520 nm, whereas the n-i-n device reaches 3.7 A/W. This ~15-fold difference indicates that the n-i-n device surpasses the traditional unity-gain limit and enters the field-induced multiplication regime.

To further explore the electric field dependence of the multiplication gain, we evaluated the EQE evolution of the device by varying biases from 0 V to -3.2 V, as plotted in **Figure 2c**. At low-bias from 0 V to -0.2 V, the device operates as a conventional photodiode, with a maximum EQE below 100%. As the bias increases beyond -0.2 V, the EQE increases nonlinearly and exceeds 1400% at -3.2 V. This bias-dependent turn-on behavior of EQE perfectly aligns with the extreme sensitivity of tunneling probability to electric fields, and indicates a field-induced multiplication process.

Generally, photomultipliers with ultra-high gain, for example, the traditional trap-mediated devices, are highly affected by trap saturation and electric field screening under high illumination intensity, which limits their linear response and thus results in

poor linear dynamic range (LDR) of around 60-80 dB. Nevertheless, across a nine-decade illumination gradient, the n-i-n device overwhelmingly outperforms the p-i-n architecture in photocurrent while maintaining good linearity, reaching a wide LDR of 100 dB, as can be seen in **Figure 2d**. The simultaneous realization of ultra-high gain and an extreme dynamic range confirms that the multiplication is governed by a robust, non-saturable localized field, effectively breaking the conventional trade-off between sensitivity and dynamic range.

Despite this gain, the response speed remains comparable to that of the p-i-n device. As can be seen in **Figure 2e**, the p-i-n device, relying merely on rapid charge sweep-out from the depletion region, exhibits fast rise/fall times of 10 μs and 243 μs. By comparison, the n-i-n device demonstrates rise and fall times of 33 μs and 387 μs, respectively. The slower fall time reflects capacitive charging and discharging as photogenerated holes accumulate at and dissipate from the heterojunction interface. Gain mechanisms based on deep traps usually show persistent photoconductivity, with response times of hundreds of milliseconds or longer. The 33 μs rise time indicates that the amplification comes from fast modulation of the local electric field rather than from slow deep traps. To further evaluate the dynamic performance in the frequency domain, we measured the normalized alternating current (AC) photoresponse as a function of modulation frequency. Consistent with the transient characteristics, the n-i-n device exhibits a -3 dB cutoff frequency of 1.47 kHz, close to the 2.93 kHz bandwidth of the conventional unity-gain p-i-n photodiode (**Supplementary Fig. 5**).

Furthermore, the effective suppression of interfacial leakage by the asymmetric barrier keeps the n-i-n device at an ultra-low shot noise floor over 1-1000 Hz (**Supplementary Fig. 6**). Remarkably, the noise current density of the n-i-n architecture is firmly restricted at 6.6×10^{-13} A $Hz^{-0.5}$, close to the 6.3×10^{-13} A $Hz^{-0.5}$ of the traditional p-i-n device, showing the photomultiplication is achieved without sacrificing the device noise. Consequently, the asymmetric n-i-n device yields a signal-to-noise ratio (SNR) of 75.1 dB under 500 Hz modulation, shown in **Figure 2f**, successfully outperforming the 74.2 dB of the p-i-n device, as seen in **Supplementary Fig. 7**.

To quantify the intrinsic detection floor and sensitivity of the device in low illumination conditions, we analyzed the noise equivalent power (NEP) and specific detectivity (D*). The NEP directly determines the threshold of the weakest optical signal that the detector can resolve. As shown in **Supplementary Fig. 8**, limited by the

physical constraints of its photon conversion mechanism, the detection floor of the traditional p-i-n device at 1520nm is rigidly restricted at 2.5×10^{-12} W/Hz$^{0.5}$. In contrast, the asymmetric n-i-n tunneling architecture, benefiting from the suppression of dark shot noise by the deep valence band of C_{60}, alongside a high multiplication responsivity of 3.7 A/W, successfully realizes an NEP of 1.77×10^{-13} W/Hz$^{0.5}$. For an active area of 0.15 cm^2, the specific detectivity of the n-i-n device surges to 2.15×10^{12} Jones, about 14 times the 1.55×10^{11} Jones of the p-i-n device, as shown in **Figure 2g**.

To evaluate the optoelectronic performance, in **Figure 2h**, we benchmarked the specific detectivity against the response bandwidth among state-of-the-art SWIR CQD photodetectors, more detailed performance parameters are given in **Supplementary Table 1**. Unlike trap-assisted photomultipliers that suffer from severe bandwidth degradation, this asymmetric n-i-n architecture achieves a remarkable balance, with both high sensitivity and rapid dynamic response. Furthermore, toward monolithic integration into large-scale arrays, device-to-device reproducibility is paramount as well. As statistically summarized in **Figure 2i**, the performance distribution of 40 discrete n-i-n devices exhibits exceptional uniformity, with both the dark current and EQE tightly gathered around their median values, which supports the fabrication of focal plane arrays.

Having established the performance advantages of this asymmetric architecture, we further investigated the profound impact of device symmetry on the multiplication physics. In the fully symmetric ITO/ZnO/PbS/ZnO/Ag structure (**Supplementary Fig. 9**), although facile bidirectional electron injection yields an EQE of 750%, the lack of a deep-valence-band layer to confine holes leads to a dark current of 1.67 mA cm^{-2} at -0.5 V, which makes the device unsuitable for weak-light detection. Similarly, the symmetric ITO/SnO_2/PbS/SnO_2/Ag structure (**Supplementary Fig. 10**) also suffers from severe leakage current, with a maximum EQE barely reaching 318%. Furthermore, devices lacking the bottom ZnO layer perform worse, with an EQE below 75%, as shown in **Supplementary Fig. 11**. Interestingly, if C_{60} is introduced on both sides of the PbS to form a dual-blocking structure, the EQE declines to 120%, shown in **Supplementary Fig. 12**.

To further establish that the observed photomultiplication originates from the engineered interfacial band alignment rather than measurement artifacts, we fabricated a control n-i-n device using smaller-size PbS QDs to systematically modify the interfacial energetics. The conduction band minimum of the small-size QDs shifts

upward, and this severe band misalignment cuts off the electron tunneling injection pathway from the ZnO layer. Consequently, as can be found in **Supplementary Fig. 13**, the photomultiplication is entirely extinguished, with a maximum EQE of 17.3% at 980 nm under -1 V, and the device reverts to a conventional photovoltaic mode driven by the built-in potential. This reveals that the gain is controlled by a specific injection window rather than bulk photoconductivity. Shifting the conduction band upward closes the window and removes the tunneling path. Therefore, only precise interfacial band alignment combined with the asymmetric architecture is the optimal strategy to obtain high gain and low noise together.

To validate the generalizability of this asymmetric physical architecture toward longer wavelengths, we replaced the absorber layer with narrower-bandgap 1650 nm PbS quantum dots. Narrow-bandgap materials usually have high thermally excited carrier concentrations, which lead to large dark currents and non-radiative recombination. However, the 1650 nm n-i-n device in this work still demonstrates outstanding photomultiplication performance. The J-V curves in **Supplementary Fig. 14a** show a dark current of 0.019 mA cm^{-2} at -0.5 V, with good rectification. Under illumination, the device gives a saturated photocurrent of up to 250 mA cm^{-2} under both forward and reverse bias. Besides, its maximum EQE reaches 907% and remains 95.6% at 1650 nm, as shown in **Supplementary Fig. 14b**, indicating that the architecture can be extended to other wavelengths.

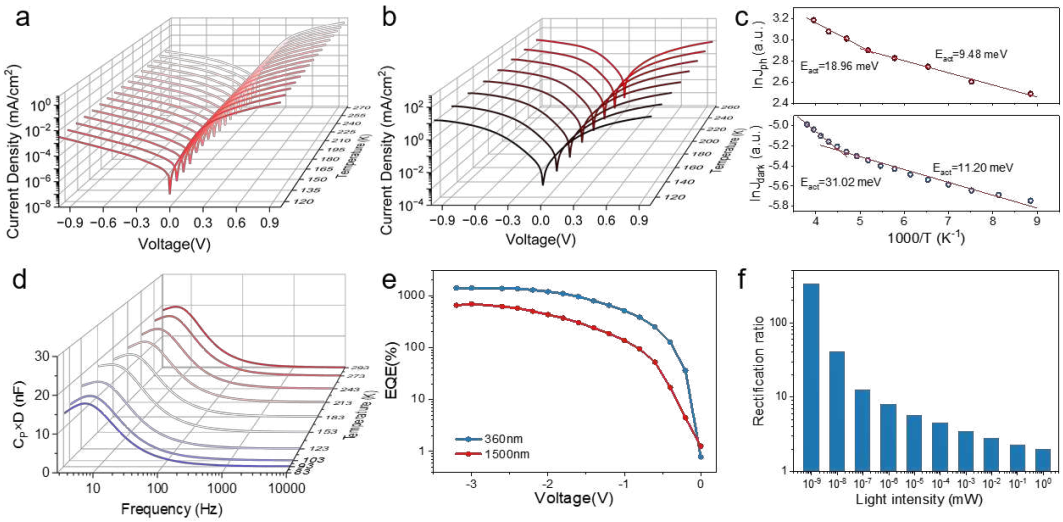


Figure 3. Characterizations of charge transport. Temperature-dependent J-V curves of the n-i-n device in (a) dark and (b) illuminated conditions. (c) Arrhenius linear fitting under dark and illumination conditions. (d) Temperature-dependent dielectric relaxation spectra from 293 K down to 83 K. (e) Bias-dependent EQE under 360 nm and 1500 nm illuminations. (f) Rectification ratio evolution of the device under varying incident light intensities.

To gain insight into the physical origins of the device's high-gain and low-noise characteristics, we systematically investigated the thermodynamic and kinetic barrier relationships of charge transport through temperature-dependent electrical characterizations. **Figure**s **3a** and **3b** present the temperature-dependent J-V curves of the device in dark and illuminated conditions, the curves are nearly independent of temperature, especially at low temperature, which completely rules out carrier freeze-out effect. **Figure 3c** shows the Arrhenius linear fitting results of the temperature-dependent J-V curves, the effective transport activation energy (E_a) extracted in the dark condition is only 11.20 meV. Under optical excitation, the dynamic modulation of the localized potential by accumulated interfacial charges further reduces the activation energy to 9.48 meV. At a room temperature of 300 K, the background thermal fluctuation energy of the lattice is approximately 25.8 meV. Such a small activation energy is difficult to reconcile with thermionic emission, which requires phonon assistance or thermal fluctuation to overcome the barrier.

Furthermore, the temperature-dependent dielectric relaxation spectra in **Figure 3d** provide further evidence for this athermal process. The characteristic peak position in the spectrum directly reflects the characteristic kinetic frequency of carriers crossing the barrier. In deep-trap mediated mechanisms, carrier freeze-out triggered by declining temperatures would cause the relaxation peak to drift towards lower frequencies. In contrast, in our device, the peak shows no measurable frequency shift between 293 and 83 K. Corresponding C_P-f spectrum confirms this as well. As can be seen in **Supplementary Fig. 15**, its massive capacitance plateau in the low-frequency region verifies the steady-state accumulation of high-density holes at the interface. This insensitivity of transport to temperature is consistent with tunneling driven by a local electric field.

The bias-dependent EQE shown in **Figure 3e** also aligns with this tunneling physical model. The EQE curves under 360 nm illumination which represents strong shallow absorption, and under 1500 nm illumination which represents weak bulk absorption, have nearly the same shape, confirming the generation of gain is uniformly governed by the interfacial localized electric field, independent of the spatial distribution of photogenerated carriers. Furthermore, **Figure 3f** shows the rectification ratio of the device, exhibiting a declining trend with increasing incident light intensity. Under reverse bias, photogenerated holes are blocked by the C_{60} barrier and undergo accumulation at the ZnO/PbS heterojunction interface. This high-density positive

charge acts as a virtual gate, inducing an enhancement of the interfacial field and narrowing the barrier width so that electrons can tunnel in. The resulting nonlinear increase in reverse current makes the reverse conductance approach the forward level, so the rectification weakens as the device moves from a rectifying contact to a tunneling multiplication state.

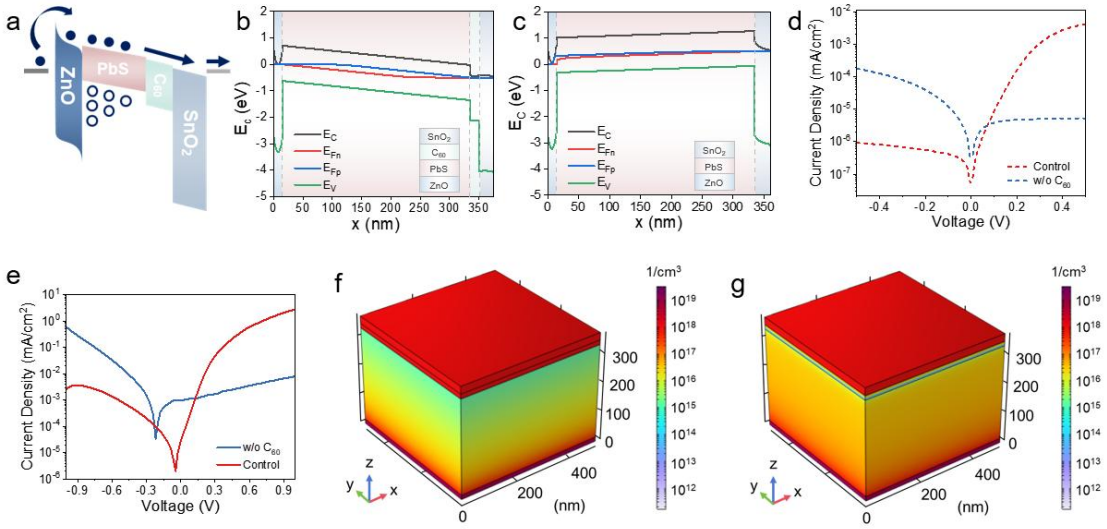


Figure 4. Simulations of energy band and spatial charge distribution. (a) Schematic illustration of the asymmetric energy band alignment. SCAPS simulated energy band diagram (b) with C_{60} layer under -0.5 V and (c) without C_{60} layer under 0.5 V, both in dark condition. (d) SCAPS predicted and (e) experimental J-V curves of devices with and without the C_{60} layer. COMSOL simulation of electron concentration at (f) zero-bias and (g) -1 V reverse bias.

To elucidate the physical mechanism of the device dynamics, we simulated the energy band under varying biases. The fundamental precondition for triggering the exceptional rectification and multiplication performance lies in constructing an asymmetric energy band alignment, as illustrated in **Figure 4a**. In the dark-state SCAPS simulations, the conduction and valence bands of the PbS region have a steeper slope when the C_{60} layer is present (**Figure 4b**). Under reverse bias, the deep valence band of C_{60} instantly functions as an ideal, high-impedance hole blocking layer. This barrier effectively suppresses dark current leakage, and converts the applied bias into an electric field across the PbS layer, which separates photogenerated charges and creates the barrier conditions for electron tunneling.

In contrast, if the C_{60} layer is removed, the band mismatch between PbS and SnO_2 induces a drastic energy spike at their interface, which can be seen in **Figure 4c**. This spike impedes electron injection under forward bias and reduces the forward current.

Concurrently, under the reverse bias, the absence of the crucial hole-confinement barrier allows massive parasitic leakage to screen the applied electric field, resulting in a flattened energy band gradient within the PbS absorption layer, shown in **Supplementary Fig. 16**. The combination of suppressed forward injection and increased reverse leakage results in a rectification inversion. **Figure 4d** presents the prediction of a multi-order of magnitude surge in the reverse dark current. Remarkably, this prediction is verified by our control experiments, as depicted in **Figure 4e**, removing the C_{60} barrier completely inverts the rectification behavior and increases the leakage current, in agreement with the physical simulations.

It is worth mentioning that energy level alignment and space-charge distribution matter as well. We replaced the core C_{60} layer with a conventional fullerene derivative, PCBM. As shown in **Supplementary Fig. 17**, although the dark current remains at a low level, the EQE at -1 V experiences a huge drop to 37%. We attribute this to the shallower LUMO of PCBM, which limits electron extraction under reverse bias and causes interfacial electron accumulation. The resulting space charge screens the field and weakens the local field at the ZnO/PbS interface. What's more, an overly thin C_{60} barrier would induce the leakage current, as is shown in **Supplementary Fig. 18**. In device employing an ultra-thin 3 nm C_{60} layer, the maximum EQE still reaching 680%, however, noticeable attenuation and a slight elevation in dark current occur compared to the control device.

Furthermore, we also used COMSOL to simulate how the electron concentration evolves with bias under illumination. **Figure 4f** shows that in the zero bias equilibrium state, photogenerated electrons are predominantly distributed within the ZnO and SnO_2 layers at both ends, as well as the C_{60} layer, while the electron concentration in the PbS layer is low, reflecting the highly efficient intrinsic charge extraction characteristic of photovoltaic mode.

At a forward bias of 1 V, electrons are injected from the SnO_2 interface and penetrate the entire PbS layer, establishing a continuous, high-concentration transport channel, which is shown in **Supplementary Fig. 19**. Remarkably, when switched to a reverse bias of -1 V, the device establishes a dense electron concentration as well, as shown in **Figure 4g**. Driven by the local field from the accumulated holes at the bottom interface, electrons from the external circuit tunnel from the ZnO through the barrier and fill the PbS layer. These three-dimensional charge dynamic profiles are consistent with the nearly symmetric photocurrent output observed under forward and reverse bias.

To evaluate the practical viability and system-level performance of our athermal tunneling photomultiplication concept, we monolithically integrated the n-i-n PbS CQD architecture with a customized CMOS readout integrated circuit (ROIC) to fabricate a 640×512-pixel focal plane array (FPA), which is presented in **Figure 5a**. Unlike traditional epitaxial InGaAs sensors that rely on costly and pixel-limited indium-bump flip-chip bonding, our solution-processed CQD layers were continuously deposited directly onto the ROIC (**Figure 5b**), effectively minimizing the manufacturing footprint. **Figure 5c** shows the imaging setup using a diffuse indirect illumination.

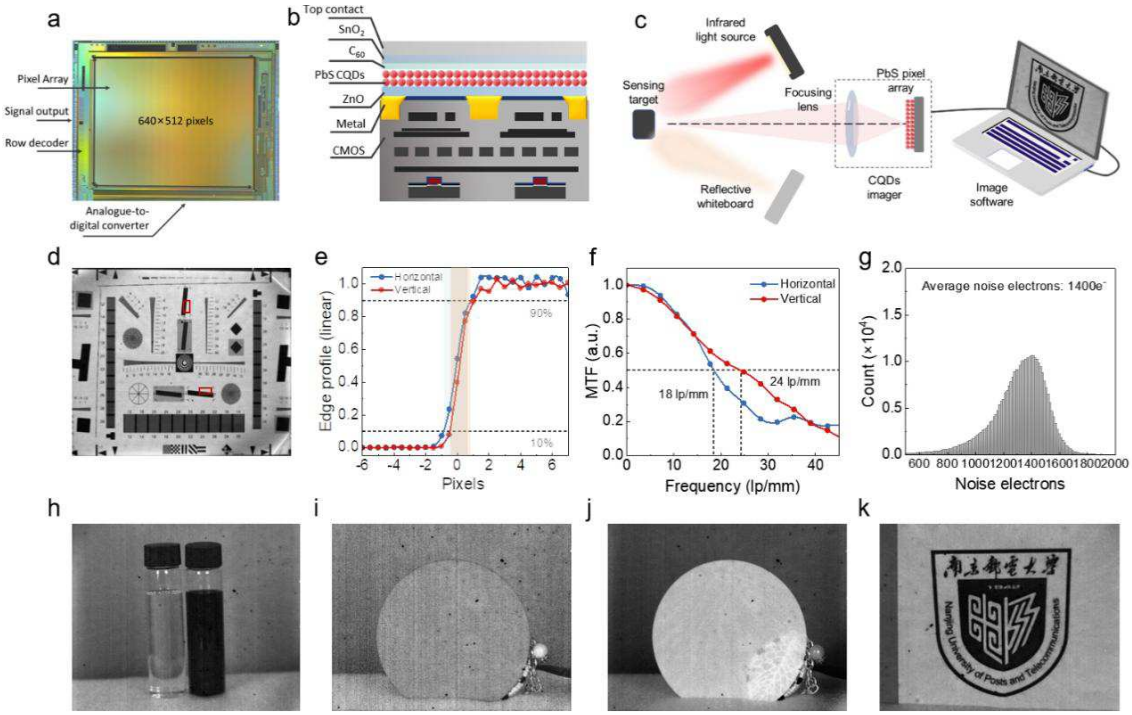


Figure 5. Monolithic integration and imaging of the short-wave infrared PbS CQD detector. (a) Photograph of the 640×512-pixel CMOS readout integrated circuit (ROIC) bare die used as the integration substrate. (b) Cross-sectional schematic of the monolithically integrated CQD imager. (c) Schematic illustration of the optical setup for imaging. (d) SWIR imaging result of the standard ISO-12233 test chart captured by the CQD imager. The red rectangles indicate the horizontal and vertical slant edges selected for spatial frequency analysis. (e) Edge spread function extracted from the slant edges in (d). (f) Modulation transfer function (MTF) of the imager. (g) Statistical distribution of the noise electrons of the imaging array. (h) SWIR imaging of two vials containing liquids that appear identical under visible light: trichloroethylene (left) and water (right). SWIR imaging of an object obscured by a silicon wafer imaged under (i) visible light and (j) 1500 nm SWIR illumination. (k) High-contrast, high-resolution SWIR image of the Nanjing University of Posts and Telecommunications logo.

Utilizing a standard ISO-12233 test chart which is exhibited in **Figure 5d**, we quantitatively assessed the spatial frequency response of the FPA. By extracting the edge spread function (ESF) from the slant edges and calculating the modulation transfer function (MTF), the imager demonstrates a 10%-to-90% signal transition spanning only 1.6 and 1.2 pixels in the horizontal and vertical directions, respectively (**Figure 5e**). Based on this exceptionally sharp edge profile, **Figure 5f** shows that the calculated MTF yields an impressive MTF50 of 18 lp/mm (horizontal) and 24 lp/mm (vertical). Furthermore, the statistical distribution of the array exhibits an average noise of only 1400 electrons (**Figure 5g**). To evaluate uniformity, in **Supplementary Fig. 20**, we mapped the pixel-to-pixel variations. The imager exhibits a photoresponse non-uniformity (PRNU) of 17.5% and a dead pixel rate of 2.67% owing to the intrinsic thickness variations of manual spin-coating. Crucially, a 0.009% hot pixel rate confirms an effective blocking of dark current and prevents localized electrical leakage across the large-area array.

Driven by this high sensitivity, the FPA enables SWIR-specific machine vision applications. Water and trichloroethylene look identical to the naked eye, but the overtone vibrational absorption of O-H bonds at 1500 nm makes water opaque while trichloroethylene remains transparent, giving strong chemical contrast. Thus, as **Figure 5h** shows, the imager separates them with ease. SWIR imaging also penetrates materials that are opaque to visible light. As **Figures 5i** and **5j** show, a crystalline silicon wafer completely blocks a visible-light camera, yet our CQD imager sees through it and recovers the object behind. We further tested resolution and real-world performance by imaging the Nanjing University of Posts and Telecommunications logo as shown in **Figure 5k**. The resulting image is sharp and distortion-free, demonstrating that our monolithic CQD CMOS device delivers both high-quality imaging and strong potential for practical use.

Conclusion

In summary, we have developed an asymmetric n-i-n colloidal quantum dot architecture that addresses the gain-versus-noise trade-off in 1500 nm SWIR sensing. By strategically integrating a C_{60} molecular barrier to construct an energetically asymmetric heterojunction, the device achieves rigorous suppression of dark leakage while enabling highly localized photo-hole accumulation at the ZnO/PbS interface. The

accumulated holes act as a virtual gate that opens an injection window and triggers athermal electron tunneling. Consequently, the device delivers an exceptional maximum EQE of over 1400%, a specific detectivity of 2.15×10^{12} Jones, and an ultra-wide linear dynamic range of 100 dB alongside a rapid response of 33 μs. This asymmetric field-driven method allowed us to monolithically integrate a 640×512 FPA which produces clear images. These results point to a straightforward path for next-generation SWIR systems including eye-safe LiDAR, night vision and non-invasive deep-tissue inspection.

Methods

Materials:

The Lead oxide (InnoChem, 99.5%), 1-Octadecene (Aladdin, >90%), oleic acid (Alfa, 90.0%), Methanol (InnoChem, 99.5%), Toluene (Nanjing Chemical Reagent Co.,Ltd, ≥99%), Oleylamine (Aladdin, >95%), phenyl isothiocyanate (TCI, ≥98%) were employed to synthesize PbS CQDs. Methanol, Trichloromethane (Nanjing Chemical Reagent Co., Ltd, >99%), Zinc acetate dihydrate (Alfa, 98%) and Potassium hydroxide (KOH) (Aladdin, 99.99%) were used to synthesize and prepare zinc oxide solvents. PbS CQD ink for active layer was prepared using lead iodide (Aladdin, 99.99%), lead bromide ($PbBr_2$) (Aladdin, 99.9%), sodium acetate (NaAc) (Aladdin, ⩾ 99.5%) and Dimethylformamide (DMF) (InnoChem, ≥99.8%).

Preparation of ZnO Nanoparticles:

Dissolve 2.96 g of zinc acetate dihydrate ($Zn(CH_3COO)_2\cdot2H_2O$) in 160 mL of anhydrous methanol to prepare a soluble zinc solution. Transfer the solution into a 250 mL three-neck flask equipped with a condenser. Stabilize the system temperature at 60°C. Dissolve 1.48 g of potassium hydroxide (KOH) in 32.5 mL of anhydrous methanol. Once the system temperature stabilizes at 60°C, slowly add the alkaline solution via a constant-pressure funnel at a uniform rate, ensuring complete addition within 10–15 min. Maintain the temperature at 60°C for 3 h after addition. Remove the heat source and let the mixture stand at room temperature for 180 min. After settling, carefully decant the supernatant. Redisperse the precipitate in methanol, transfer to a centrifuge tube, and centrifuge at 2500 rpm for 3 min. Quickly discard the supernatant, add anhydrous methanol, vortex for 60 s, and centrifuge at 6000 rpm for 2 min. Discard the supernatant, add 20 mL of an equal-volume mixture of anhydrous methanol and

chloroform to the centrifuge tube. Vortex to homogenize, filter through a 0.45 μm polytetrafluoroethylene (PTFE) syringe filter, and store in a low-temperature, light-protected environment.

Synthesis and Purification of PbS CQDs:

In a glovebox, weigh 0.9 g of lead oxide (PbO), 30 ml of 1-octadecene (ODE), and 2.45 ml of oleic acid (OA) using an electronic balance, and transfer into a 100 mL three-neck flask. Seal the flask, remove from the glovebox, and degas under vacuum with stirring at room temperature for 30 minutes. Maintain vacuum and set the thermostatic heating magnetic stirrer to 120°C. Raise the solution temperature to 135°C. In the glovebox, prepare a thiourea precursor by dissolving 2.28 g of phenyl isothiocyanate and 4.51 g oleylamine (OAm) in 3.21 g of ODE. Once the temperature stabilizes at 135°C, switch to a nitrogen atmosphere. Rapidly inject the thiourea precursor into the flask. After 20 minutes of reaction, immediately remove the heat source and allow the solution to cool to room temperature. Quench the reaction by adding 100 mL of acetone. Stir for 5 minutes, transfer the mixture into centrifuge tubes, and centrifuge at 6000 rpm for 5 minutes. Discard the supernatant. Transfer the centrifuged PbS CQDs solid back into the glovebox. Add 10 mL of n-hexane to the centrifuge tube containing PbS CQDs and vortex until fully dissolved. Prepare a mixture of 10 mL ethanol and 15 mL ethyl acetate, add it to the n-hexane solution, vortex for 2 minutes, and centrifuge at 4000 rpm for 3 minutes. Repeat this step twice. Dry the centrifuged colloidal quantum dots under vacuum, weigh the solid, and dissolve in n-hexane to prepare a 50 mg/mL solution.

Ligand Exchange Method for Preparing PbS CQDs Ink:

Prepare ligand exchange solution: Dissolve 0.1 M lead iodide (PbI_2), 0.04 M lead bromide ($PbBr_2$), and 0.044 M sodium acetate (NaAc) in DMF. Vortex until fully dissolved. Dilute 0.7 mL of pre-prepared 50 mg/mL PbS quantum dot (QD) solution to 1.67 mg/mL in a centrifuge tube and mix thoroughly. Add 5 mL of the prepared exchange solution, vortex vigorously to facilitate ligand exchange, and allow QDs to transfer into the DMF phase. After phase separation, discard the upper layer. Wash the remaining solution with 20 mL of n-hexane, vortex, and repeat twice to remove by-products. Discard the upper layer, add 3 mL of toluene to the remaining solution, vortex, and centrifuge at 4000 rpm for 3 min.

Fabrication Process of PbS Photodetector:

Clean ITO-coated conductive glass by immersing it in a surfactant aqueous

solution and sonicating for 15 minutes. Rinse once with ultrapure water. Sequentially sonicate the ITO in acetone and isopropanol for 15 minutes each. Dry in an oven at 60 °C. Deposit 70 μL of pre-prepared ZnO nanoparticle solution via spin-coating at 5000 rpm to form the ZnO film. Deposit 45 μL of pre-prepared QD ink via spin-coating at 1800 rpm to form the photoactive layer. Place the device on a shadow mask and load it into a vacuum evaporator. Evacuate to 5×10^{-4} Pa, then thermally evaporate C_{60}. Deposit 15 nm of C_{60} at a rate of 0.2 Å/s. Deposit 25 nm of SnO_2 by Atomic Layer Deposition (ALD). Load the device into the vacuum evaporator. Evacuate to 5×10^{-4} Pa, then thermally evaporate silver (99.9999 %). Deposit 20 nm of Ag at an initial rate of 0.1 Å/s, followed by 80 nm at 0.9 Å/s, achieving a total 100 nm Ag electrode.

Materials Characterization

The absorption spectra were measured by PerkinElmer Lambda 650. XPS measurements were performed on Shimadzu Axis Supra. UPS measurements were performed using a He gas discharge lamp emitting He I radiation ($h\nu$ = 21.22 eV) with a pass energy of 10 eV and a bias of -9 V to ensure secondary electron onset detection. Cluster etching was performed using large Ar clusters generated by the GCIS Ion Source (Kratos Analytical Inc.) with an energy of 10 keV. The cross-section image of the device was investigated using a Hitachi S-4800 SEM. The TEM image was acquired by Hitachi HT7700.

Devices Characterization

The I-V curves and other current-related data were recorded by Keysight B2912B precision source/measure unit (SMU) (part of the B2900B series). The EQE and responsivity spectra were measured by QE-R system from Enlitech Co., Ltd. The noise current was extracted from the Rigol DHO 1000 through a trans-impedance amplifier (TIA). The rise and decay times were obtained by an oscilloscope with a function generator controlling the frequency of light source. The square waveform voltage with different frequency was applied by a function generator (Rigol DG 800 Pro). Temperature-dependent capacitance–frequency measurement was performed using an electrochemical workstation analyzer (CHI600E) with an AC signal, temperature was controlled through liquid nitrogen.

Data availability

All data generated or analyzed during this study are included in the published article and its Supplementary Information. Additional data are available from the corresponding author on request. Source data are provided with this paper.

References

1 Hu, H. *et al.* Double-Heterojunction-Based HgTe Colloidal Quantum Dot Imagers. *ACS Nano* **19**, 8974-8984 (2025).

2 Lei, R. *et al.* A Separate-Absorption-Charge-Multiplication Short-Wave Infrared Avalanche Photodiode With an Ultrahigh Gain Based on PbS Quantum Dots. *Laser & Photonics Reviews* **20**, e03091 (2026).

3 Tran, H.-C. V. *et al.* Enhanced SWIR Photodetection in Colloidal Quantum Dot Photodiodes via Tunneling Current Suppression. *ACS Appl. Mater. Interfaces* **17**, 15666-15674 (2025).

4 Sordillo, D., Sordillo, L., Sordillo, P., Shi, L. & Alfano, R. Short wavelength infrared optical windows for evaluation of benign and malignant tissues. *J. Biomed. Opt.* **22**, 045002 (2017).

5 Wang, Y. *et al.* Silver telluride colloidal quantum dot infrared photodetectors and image sensors. *Nat. Photonics* **18**, 236-242 (2024).

6 Roblyer, D. *et al.* Review of shortwave infrared imaging and spectroscopy in tissue. *Biomed. Opt. Express* **16**, 5028-5062 (2025).

7 Zhu, B. & Jonathan, H. A Review of Image Sensors Used in Near-Infrared and Shortwave Infrared Fluorescence Imaging. *Sensors* **24**, 3539 (2024).

8 Pi, H. *et al.* Infrared Photodetectors Based on Silver Chalcogenide Colloidal Quantum Dots. *Advanced Optical Materials* **13**, 2403489 (2025).

9 Ba, K. & Wang, J. Advances in solution-processed quantum dots based hybrid structures for infrared photodetector. *Materials Today* **58**, 119-134 (2022).

10 Leemans, J. *et al.* Colloidal III–V Quantum Dot Photodiodes for Short-Wave Infrared Photodetection. *Advanced Science* **9**, 2200844 (2022).

11 Pang, C. *et al.* Integrated PbS Colloidal Quantum Dot Photodiodes on Silicon Nitride Waveguides. *ACS Photonics* **10**, 4215-4224 (2023).

12 Zhan, S. *et al.* High responsivity colloidal quantum dots phototransistors for low-dose near-infrared photodetection and image communication. *Light: Science & Applications* **14**, 201 (2025).

13 Wang, Y. *et al.* Colloidal PbS Quantum Dot Photodiode Imager with Suppressed Dark Current. *ACS Appl. Mater. Interfaces* **15**, 58573-58582 (2023).

14 Zhao, X. *et al.* Lead Chalcogenide Colloidal Quantum Dots for Infrared Photodetectors. *Materials* **16**, 5790 (2023).

15 Nakotte, T., Luo, H. & Pietryga, J. PbE (E = S, Se) Colloidal Quantum Dot-Layered 2D Material Hybrid Photodetectors. *Nanomaterials* **10**, 172 (2020).

16 Wang, H. *et al.* Stable P-Type PbS Quantum Dot Ink for all-Blade-Coated Short-Wavelength Infrared Photodiodes. *Adv. Mater.* **38**, e18118 (2026).

17 Konstantatos, G. *et al.* Ultrasensitive solution-cast quantum dot photodetectors. *Nature* **442**, 180-183 (2006).

18 Ackerman, M. M., Tang, X. & Guyot-Sionnest, P. Fast and Sensitive Colloidal Quantum Dot Mid-Wave Infrared Photodetectors. *ACS Nano* **12**, 7264-7271

(2018).
19 Kwon, J. B., Han, M., Jung, D. G., Kong, S. H. & Jung, D. High Sensitivity Shortwave Infrared Photodetector Based on PbS QDs Using P3HT. *Nanomaterials* **11**, 2683 (2021).
20 Wei, Y. *et al.* Hybrid Organic/PbS Quantum Dot Bilayer Photodetector with Low Dark Current and High Detectivity. *Adv. Funct. Mater.* **28**, 1706690 (2018).
21 Yang, M., Liu, H., Wen, S., Du, Y. & Gao, F. Optimizing the Infrared Photoelectric Detection Performance of Pbs Quantum Dots through Solid-State Ligand Exchange. *Materials* **15**, 9058 (2022).
22 Peng, M. *et al.* Room-Temperature Direct Synthesis of PbSe Quantum Dot Inks for High-Detectivity Near-Infrared Photodetectors. *ACS Appl. Mater. Interfaces* **13**, 51198-51204 (2021).
23 Wang, H., Kubo, T., Nakazaki, J. & Segawa, H. Solution-Processed Short-Wave Infrared PbS Colloidal Quantum Dot/ZnO Nanowire Solar Cells Giving High Open-Circuit Voltage. *ACS Energy Letters* **2**, 2110-2117 (2017).
24 Wang, X. *et al.* Amorphous ZnO/PbS Quantum Dots Heterojunction for Efficient Responsivity Broadband Photodetectors. *ACS Appl. Mater. Interfaces* **12**, 8403-8410 (2020).
25 Zhang, J.-Y., Xu, J.-L., Chen, T., Gao, X. & Wang, S.-D. Toward Broadband Imaging: Surface-Engineered PbS Quantum Dot/Perovskite Composite Integrated Ultrasensitive Photodetectors. *ACS Appl. Mater. Interfaces* **11**, 44430-44437 (2019).
26 Kim, B. *et al.* Ultrahigh-gain colloidal quantum dot infrared avalanche photodetectors. *Nat. Nanotechnol.* **20**, 237-245 (2025).
27 Gong, W., Wang, P., Li, J., Li, J. & Zhang, Y. Elucidating the Gain Mechanism in PbS Colloidal Quantum Dot Visible–Near-Infrared Photodiodes. *The Journal of Physical Chemistry Letters* **13**, 8327-8335 (2022).
28 Konstantatos, G. & Sargent, E. H. PbS colloidal quantum dot photoconductive photodetectors: Transport, traps, and gain. *Appl. Phys. Lett.* **91** (2007).
29 Xu, K. *et al.* Large Photomultiplication by Charge-Self-Trapping for High-Response Quantum Dot Infrared Photodetectors. *ACS Appl. Mater. Interfaces* **14**, 14783-14790 (2022).
30 Han, S. G. *et al.* Photomultiplication-Type Organic Photodetectors with Fast Response Enabled by the Controlled Charge Trapping Dynamics of Quantum Dot Interlayer. *Adv. Funct. Mater.* **31**, 2102087 (2021).
31 Jeong, M. *et al.* Photomultiplication-Type Organic Photodetectors with High EQE-Bandwidth Product by Introducing a Perovskite Quantum Dot Interlayer. *Adv. Funct. Mater.* **33**, 2300695 (2023).
32 Bai, H. *et al.* High-performance photomultiplication-type quantum dot IR photodetectors at low applied voltages. *Journal of Materials Chemistry C* **13** (2025).
33 Li, J.-L. *et al.* Photomultiplication Enables Efficient NIR Quantum Dot Organic

Upconversion Devices. *ACS Photonics* **13**, 1456-1464 (2026).

34 Zhang, X., Zhang, N. & Xu, X. Tuning the Photoresponse Mode of PbS Quantum Dot Homojunction Photodetectors. *ACS Applied Nano Materials* **9**, 712-720 (2026).

35 Chen, B. *et al.* Low Dark Current High Gain InAs Quantum Dot Avalanche Photodiodes Monolithically Grown on Si. *ACS Photonics* **7**, 528-533 (2020).

36 Yan, Q. *et al.* Trap-Assisted Tunneling in PbS Colloidal Quantum Dots Photodetector. *IEEE Trans. Electron Devices* **71**, 6085-6090 (2024).

37 Hammond, W. T. & Xue, J. Organic heterojunction photodiodes exhibiting low voltage, imaging-speed photocurrent gain. *Appl. Phys. Lett.* **97**, 073302 (2010).

38 Yanikgonul, S. *et al.* Integrated avalanche photodetectors for visible light. *Nat. Commun.* **12**, 1834 (2021).

39 Wang, Y. *et al.* Ultrahigh Gain Solar Blind Avalanche Photodetector Using an Amorphous Ga2O3-Based Heterojunction. *ACS Nano* **15**, 16654-16663 (2021).

Acknowledgments

This work was financially supported by National Key R&D Program of China (2024YFB3614401), National Natural Science Foundation of China (62374091), the Project of State Key Laboratory of Organic Electronics and Information Displays, Nanjing University of Posts and Telecommunications (No. GZR2024010029, GZR2023010018), Nanjing University of Posts and Telecommunications (Start-up Grant: NY223179, NY224074), Natural Science Foundation of Jiangsu Province (BK20240634), Universities Natural Science Foundation of Jiangsu Province (24KJB510024).

Author contributions

Z.H, B.Z., and C.D. contributed equally to this work.

B.S., L.G. and M.W. conceived and supervised the project. Z.H. synthesized the PbS colloidal quantum dots, fabricated the photodetectors and carried out the structural and optoelectronic characterization. B.Z. and H.Z. performed the ultraviolet and X-ray photoelectron spectroscopy measurements and the SCAPS device simulations. T.M. and M.L. contributed to device fabrication, ligand exchange and data analysis. J.L. performed the COMSOL three-dimensional simulations of the charge-carrier distribution. C.D. and Y.L. designed the CMOS readout integrated circuit, and carried out the monolithic integration, focal-plane-array fabrication and imaging measurements. L.Z. and M.W. contributed to the analysis of the tunneling mechanism and to the preparation of the figures. Z.H., M.W. and B.S. wrote the manuscript with input from all authors. All authors discussed the results and commented on the manuscript.

Competing interests

The authors declare no competing interests.

Additional information

The Supporting Information is available free of charge on the …….

Experimental details regarding materials, nanoparticle synthesis, and device fabrication; Comprehensive material characterizations including X-ray diffraction (XRD), X-ray photoelectron spectroscopy (XPS), and ultraviolet photoelectron spectroscopy (UPS)

spectra; Advanced optoelectronic performance metrics including responsivity, response bandwidth, noise power density, signal-to-noise ratio, and noise equivalent power (NEP) spectra; comprehensive optoelectronic data (J-V and EQE) for various control devices: symmetric structures, varying quantum dot sizes, and alternative transport layers; Capacitance-frequency spectra; theoretical simulations including SCAPS energy band alignments and COMSOL 3D electron concentration profiles; and pixel-level statistical scatter plots of the focal plane array.

Supplementary Files

This is a list of supplementary files associated with this preprint. Click to download.

- SI20261013NatPhotonics.docx